Quasi-classical model of non-destructive wavepacket manipulation by intense few-cycle nonresonant laser pulses

Contact *w.a.bryan@swansea.ac.uk*

W A Bryan and G R A J Nemeth

Department of Physics
Swansea University
Singleton Park, Swansea SA2 8PP

C R Calvert, R B King, J B Greenwood and I D Williams

Department of Pure and Applied Physics
Queen's University Belfast, BT7 1NN

W R Newell

Department of Physics and Astronomy
University College London
London WC1E 6BT

Introduction

This article follows a recent publication [1]. To quantify the observations of femtochemistry and coherent control, novel theoretical treatments were developed to accurately quantify the evolution of nuclear wavepackets created and controlled by the light–matter interaction. At low intensities (generally $I < 10^{10}$ Wcm^{-2}), the evolution of a nuclear wavepacket can be described by the perturbation theory and the population of the initial state is assumed to be constant [2].

In the intermediate intensity regime (defined as 10^{10} $Wcm^{-2} < I < 10^{12}$ Wcm^{-2}), the population of the initial and final states must be considered; the intensity regime is also dependent on the coupling strength between the electronic states. The analytical solution of the Schrödinger equation is often impossible, hence numerical integrations or alternative representations of wavepackets are required: quasi-classical trajectories are often employed, which may be intuitively understood [3].

In the strong-field regime, which we define as $I > 10^{13}$ Wcm^{-2}, multiphoton or tunnel ionization become highly probable processes in atoms, and photodissociation and Coulomb explosion become dominant in molecules. Studying these processes has led to a significant advancement in understanding the dynamic structure of small molecules in intense laser fields, as recently reviewed by Posthumus [4]. While the interference of quantum pathways occurs under such conditions, it is often more useful and intuitive to think in terms of laser-induced dipole forces. The electric field induced by the laser field is sufficiently strong that atomic and molecular orbitals are polarized and impulsive Raman processes are possible [5]. The propagation of liberated electrons in the laser field should also be considered, particularly in the case of high harmonic generation (see [6] and references therein).

Under strong-field conditions it might seem unlikely that the delicate finesse required for quantum control would be possible; however, by applying the control pulse for a time significantly shorter than the fastest vibrational or rotational motions, the electronic structure of the molecule can be modified. This alters the environment in which the nuclei move, changing the motion of the nuclear wavepacket. An additional advantage is that ionization and fragmentation become less likely with shorter control pulses.

With the advent of few-cycle near infrared (NIR) laser pulses, a number of experimental groups have carried out studies to characterize vibrational wavepackets in hydrogenic molecular ions as recently reviewed by the authors [7]. Following illumination by an ultrafast strong-field pump, tunnel ionization of neutral H_2 or D_2 molecules leads to the formation of molecular ions supporting vibrational wavepackets. Such targets are attractive as they are theoretically tractable, and hence the Schrödinger equation can be solved within the Born–Oppenheimer and dipole approximations. Furthermore, the excited electronic states are isolated from the ground state of the D_2^+ ion, and hence electronic excitation is negligible. As is often true of vibrational wavepackets in diatomic molecules, the anharmonicity of the potential energy surface causes the wavepacket to dephase, dissipating the vibrational state components over a range of internuclear separations within a few classical periods. Theoretical predictions were recently confirmed experimentally, as reviewed by Calvert et al [7].

Just as femtochemistry led to quantum or coherent control, the observation of nuclear dynamics in strong-field few-cycle pulses also opens possibilities for analogous manipulation of the quantum state of molecules. Niikura *et al* have employed NIR laser pulses to perform experimental investigations of the laser-induced dipole forces to influence vibrational motion [8] in H_2^+ and D_2^+ , focusing on measuring the ion fragmentation energy as the pump-control delay is varied. Thumm and co-worker have reported an accurate quantum mechanical treatment of a vibrational wavepacket [9] and the influence of an ultrashort control pulse [10]. The authors in collaboration with Murphy and McCann have used a similar numerical treatment to investigate the heating and cooling of vibrational populations [11], recently leading to the prediction of the 'quantum chessboard' effect [12].

The QCM is broken into a series of steps. The creation of a coherent superposition of states is modelled by extending the non-adiabatic ionization model of Yudin and Ivanov [13] to a molecular system, allowing the vibrational state population to be evaluated. A non-interacting classical ensemble is then created, with weighted quantized vibrational levels to reflect the initial state of the molecule. The wavepacket evolution is then approximated by allowing the classical ensemble to propagate on the internuclear potential energy surface (PES). Now, applying a 'control' pulse to the propagating ensemble causes a time-dependent deformation of the PES [8]: the large gradient of the induced electric field causes a large AC Stark shift. Essentially, the interaction of the induced field and the electron orbital causes a force on the nuclei. The resulting deformation of the potential accelerates or decelerates components of the ensemble depending on their direction of motion, transferring energy into or out of the system. The influence of this energy transfer is twofold, changing the relative phase of the ensemble components with respect to the unperturbed system, and transferring population between vibrational states. The transfer of population is considered to occur when the motion of an ensemble component is sufficiently perturbed by the control pulse that it takes on the characteristics of a higher- or lower-lying vibrational state (i.e. amplitude and frequency). Each of these processes is discussed below.

Molecular ionization in a few-cycle pulse

The MO-ADK (molecular orbital Ammosov–Delone–Krainov) formulation [14] has been relatively successful in predicting ionization rates; however, any theory that makes use of the original ADK treatment [15] is not ideally suited for a few-

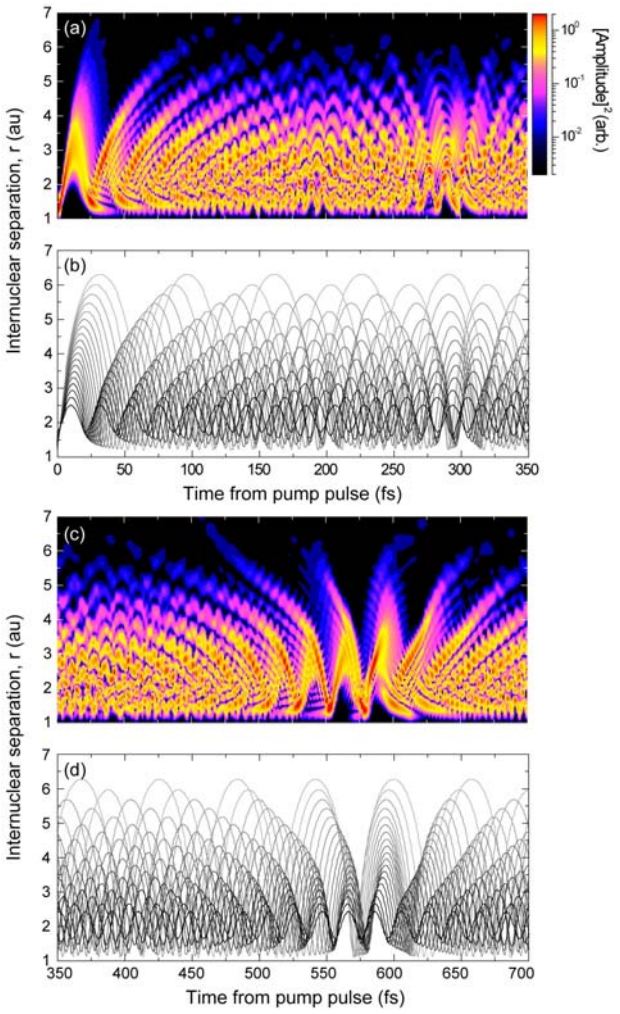

Figure 1. Comparison between the time-dependent solution of the Schrödinger equation for the evolution of the vibrational wavepacket (v = 0–18) in D+ 2 (a, c, colour panels) and the QCM model (b, d, trajectories). The initial dephasing (a and b) and revival (c and d) of the vibrational wavepacket is shown. The QCM reproduces the features of the TDSE solution, as there is a bunching of the trajectories in regions where the solution of the TDSE is localized. The false colour panels are on a logarithmic scale, and the grey scale of the trajectories has been adjusted to illustrate similarities.

cycle pulse, being a quasistatic approximation. Instead, here we modify the recent work of Yudin and Ivanov [13] in which an analytical expression for ionization rate is found for arbitrary values of the Keldysh parameter. The flexibility of these expressions allows us to treat ionization between electronic states of the molecule efficiently.

The distribution of vibrational states depends on the probability of ionization and the overlap between the ground state wavefunction in the neutral and the available vibrational states in the ion. The recent experimental findings of Urbain *et al* [16] and theoretical discussion by Kjeldsen and Madsen [17] identified a significant deviation from the expected Franck–Condon-like distribution of vibrational states being populated by strong-field ionization in an ultrafast NIR laser pulse. This deviation was found to be dependent on peak laser intensity: on the leading edge of the pump pulse, the $D_2 \rightarrow D_2^+$ ($1s\sigma_g$) ionization rate increases highly nonlinearly with laser intensity. The distribution of vibrational states is a direct result of the dependence of the ionization potential on internuclear separation, such that the maximum ionization rate (hence maximum population) does not necessarily occur at the optimum overlap of the ground state neutral wavepacket and the states in the molecular ion. Furthermore, once the intensity is sufficiently high to generate the molecular ion, there is also a significant excitation rate to the D_2^+ ($2p\sigma_u$) dissociative state. This is a loss channel and depopulates the number of D_2^+ ions supporting vibrational wavepackets. An additional loss channel exists in $D^+ + D^+$ Coulomb explosion, requiring a still higher intensity.

Field-free wavepacket evolution

In a manner directly comparable to the trajectory methods pioneered in femtochemistry and coherent control, we treat the evolution of the vibrational wavepacket in the molecular ion as an ensemble of classical particles moving on the bound PES.

The ionization event that launches the vibrational wavepacket enforces a coherence to the resulting motion, as the ionization rate is maximum for all vibrational states in the ion at the inner turning point. It is assumed that the unit mass of the classical particle is initially stationary following projection onto the ionic PES, which is reasonable considering that the tunnel time is much shorter than the characteristic time-scale for wavepacket propagation. We then treat the motion of each element of the ensemble as a Newtonian particle accelerated according to the differential of the PES. The presented discussion is confined to one dimension to be applicable to the hydrogenic molecular ion; however, this holds for any number of degrees of freedom, and hence has significant promise for quantifying wavepacket motion in complex polyatomics exposed to strong-field pump pulses causing excitation or ionization.

The motion of the ensemble (and hence the approximation to the wavepacket motion) is then predicted by allowing the unit masses to propagate as a function of time. The result of propagating the QCM for a typical number of vibrational states (generally from $v = 0$ to $v = 24$) is presented in figure 2, and a visual comparison made to the solution of the time-dependent Schrödinger equation (TDSE) for D_2^+ within the Born–Oppenheimer and dipole approximations, as published in [X]–[X]. Clearly, as the QCM generates a series of trajectories and the quantum treatment results in a continuous wavefunction, a direct numerical comparison is difficult. However, it is apparent from figure 2 that the QCM captures the essence of the quantum wavepacket result. This is not surprising, as both motions are the direct consequence of the PES shape as a function of R; however, this comparison is intended to indicate the convergence of the classical trajectory calculation despite only requiring 7000 simulation steps to model the wavepacket motion over 700 fs. A typical split operator propagation of the TDSE (where a solution exists) requires of the order 30 000 steps, i.e. a time-step of 1 au (24.2 as).

Figure 1 presents two subsets of the now familiar wavepacket dephasing and revival. Comparing the QCM trajectories and the predicted TDSE-derived wavepacket amplitude at 590–600 fs, the intense features in the false colour representation of the wavepacket are apparent in the overlapping or closely spaced QCM trajectories. The slightly imperfect rephasing of the wavepacket predicted by the TDSE solution is replicated in the QCM trajectories.

Quantifying deformation of the PES

In the strong-field regime, the optically induced electric field is sufficient to not only distort the PES via the Stark shift, but also to polarize the molecular orbital(s), which the nuclei experiences as a time-dependent force, therefore changing the potential energy. The orbitals respond to the electric field (i.e. on an attosecond, or at least few femtosecond time-scale), but the nuclei are only driven by the cycle-averaged envelope; hence, if a control pulse is applied to a molecule supporting a vibrational wavepacket, the nuclear motion adjusts according to the external influence. Consequentially, our control pulse will modify the effective PES by the dipole force generated by

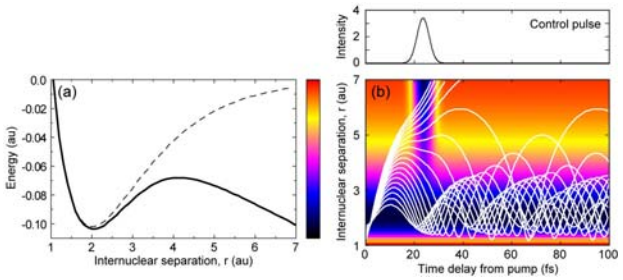

Figure 2. Potential energy surface distortion by the control pulse and associated ensemble perturbation. (a) With a control pulse intensity of $I_{control}$ = 3.5 × 10^{13} Wcm^{-2}, the 1sσ_g potential is heavily distorted (solid line) as compared to the field-free situation (dashed line). (b) The distortion of the PES as a function of time when a 7 fs control pulse is applied at 24 fs, referenced to the energy scale of (a). The trajectories predicted by the QCM are overlaid on the potential; the distortion of all trajectories is dependent on state amplitude and phase relative to the control pulse (shown in units of 10^{13} Wcm^{-2}). The maximum in the PES induced by the control pulse around 4 au present in (a) becomes a saddle point as a function of time in (b).

polarizing the molecular orbital and subsequential Stark shifting.

In figure 2(a), the field-free PES and the maximally laser-distorted PES are shown; such a dramatic deformation of the PES is only present for a fraction of the vibrational period. The distortion of the PES by the control pulse causes a time-dependent variation of dV(R)/dR, and hence the ensemble components experience an additional acceleration, the direction and magnitude of which depends on the direction the component is moving and its location on the PES. This causes a net increase or decrease of energy depending on whether the control pulse dipole force acts to enhance or retard the ensemble elements, interpreted as a change of vibrational state in a quantum representation. This is illustrated in figure 2(b), whereby a 7 fs FWHM Gaussian control pulse of peak intensity $I_{control}$ = 3.5 × 10^{13} Wcm^{-2} is applied 24 fs after the wavepacket is created by the pump pulse (i.e. t = 0). The trajectories around R = 5 au at 24 fs illustrate this point well: both are accelerated to larger R under the influence of the control.

Variation of vibrational state and phase

As the ensemble of quasi-classical particles propagates, the laser-induced force transfers energy into or out of the system. Clearly, the discrete vibrational states have an influence when considering the quantum nature: a change of vibrational state only occurs when sufficient energy has been gained or lost to instigate a change in state.

As is illustrated in figure 2, the time-varying distortion of the molecular PES by the control pulse causes the component trajectories to vary from the unperturbed motion. If additional energy is transported into a trajectory, the amplitude of the oscillation increases, along with the vibrational period, and hence the trajectory takes on the characteristics of a higher-lying state. We propose that this increase in energy is equivalent to population being transferred from a lower to higher vibrational state. Similarly, the control pulse can simultaneously remove energy from the system, causing a decrease in vibrational state.

As the control pulse can up- and down-shift vibrational population, it is possible that multiple ensemble components can end up in the same vibrational state, and the phase and relative population of each state must be considered. Variations in the phase and population are quantified by making a numerical comparison between the perturbed (e.g. figure 2) and unperturbed (figure 1) trajectories. Importantly, this comparison must be made once the intensity of the control pulse has dropped to zero, such that the trajectories are only defined by

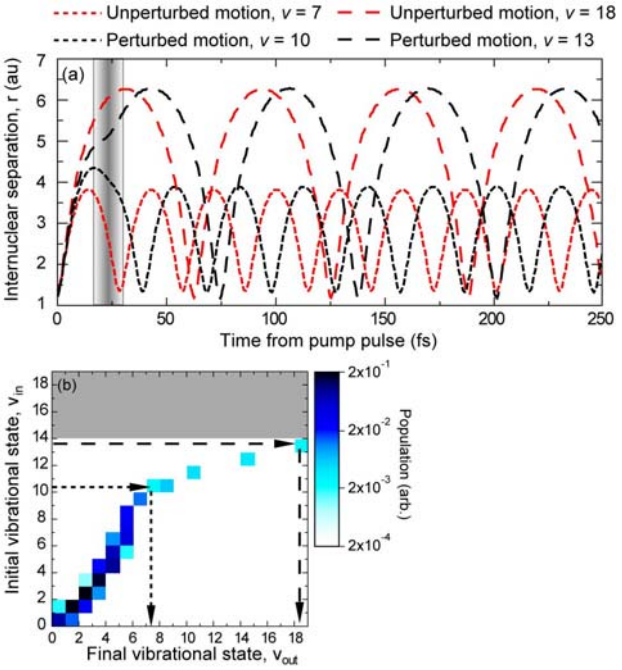

Figure 3. Vibrational population transfer in the QCM. (a) The application of a 7 fs duration control pulse with an intensity of 3.5 × 10^{13} Wcm^{-2} at 24 fs causes both positive- and negative-going population transfer. The initial state v = 10 is down-shifted into resonance with the v = 7 state by the control pulse (red and black short dashed lines), while the v = 13 state is up-shifted into resonance with the v = 18 state (red and black long dashed lines). The shaded region indicates the intensity of the control pulse and the vertical lines indicate when the intensity is 3.5 × 10^{12} Wcm^{-2}. (b) The vibrational population matrix conveniently illustrates the action of the control pulse. Each point on the matrix indicates the likelihood of population transfer on a logarithmic colour scale, and the grey region for v > 14 indicates states are no longer bound. Projecting the sum of the matrix vertically returns the final vibrational population.

the static PES. In practice, it is important to ensure that the control pulse(s) does not suffer from significant pedestals on the femtosecond and picosecond time-scale. Therefore a third-order autocorrelation contrast measurement is required when comparing with experimental results, in case an underlying PES distortion exists.

Comparison with established results

While figure 1 has demonstrated that the QCM can successfully reproduce the unperturbed motion of a vibrational wavepacket by propagating the ensemble, it could be argued that any treatment relying on the differentiation of the field-free PES will give a similar result, assuming sufficient numerical accuracy. It is therefore vital to quantify the ability of the QCM to accurately describe the action of the control pulse; to this end, we compare the output of the QCM to established theoretical results. In figure 4, systematic scans of the control delay and intensity with respect to the pump pulse are presented for direct comparison with the reproduced results of Niederhausen and Thumm, figure 5 [10]. In both cases, the control pulse is 6 fs in duration and the initial vibrational state distribution is calculated using the tunneling theory. Importantly, the initial distribution of vibrational states in [10] was calculated using the ADK treatment [15]. The TDSE was then solved within the Born–Oppenheimer approximation, andthe control pulse causes Raman transitions between vibrational states. Furthermore, following the control pulse, the wavepacket is projected onto the Coulomb explosion PES.

Despite the differences in method, a good agreement is found (especially considering how disparate the two numerical techniques are), indicating that the QCM accurately captures the

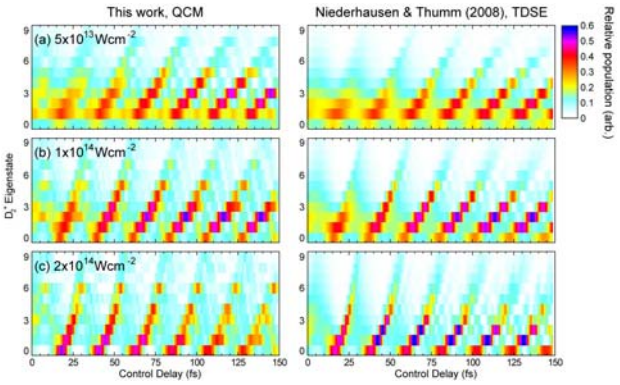

Figure 4. Final vibrational state population distributions for three different control pulse intensities as the temporal separation between the pump and control pulse is varied. The results of Niederhausen and Thumm [10] are reproduced for comparison with the QCM, which reproduces the periodicity and relative shift of vibrational population as the delay between the pump (6 fs, 10^{14} Wcm^{-2}) and the control is varied.

modification of the vibrational population as revealed by a full quantum mechanical model. Approximating the evolution of a wavepacket under the influence of an ultrafast strong-field control pulse as a quasi-classical ensemble is therefore justified.

Conclusions

A QCM has been proposed that allows the quantification of wavepacket dynamics modified by an ultrashort strong-field non-resonant laser pulse. We have discussed how the vibrational phase and population are adjusted by the control pulse, and a comparison has been made with established theoretical predictions. Systematic predictions of wavepacket dynamics as a function of pump intensity and control delay and intensity have been presented. Such results will be of interest to groups attempting to experimentally detect the manipulation of a wavepacket. Attosecond studies in complex many-electron molecules is such an application; the QCM could be employed to identify the populated electronic states suggested, whereby the coupling of electronic states in a strong field distorts the vibrational wavepackets generated, thus revealing the nuclear and electronic dynamics..

Acknowledgements

We thank Thomas Niederhausen for communicating the data used in figure X, This work was supported by the Engineering and Physical Sciences Research Council (EPSRC) and the Science and Technology Facilities Council (STFC), UK. CRC and RBK acknowledge financial support from the Department of Education and Learning, Northern Ireland; GRAJN acknowledges financial support from EPSRC and STFC.

References

1. W A Bryan, C R Calvert, R B King, G R A J Nemeth, J B Greenwood, I D Williams and W R Newell, *New J. Phys.* **12** 073019 (2010)
2. P Brumer and M Shapiro *Chem. Phys. Lett.* **126** 541 (1986), M Shapiro, J W Hepburn and P Brumer, *Chem. Phys. Lett.* **149** 451 (1988), D J Tannor and S A Rice, *J. Chem. Phys.* **83** 5013 (1985), D J Tannor, R Kosloff and S A Rice, *J. Chem. Phys.* **85** 5805 (1986).
3. R W Robinett *Phys. Rep.* **392** 1–119 (2004)
4. J H Posthumus, *Rep. Prog. Phys.* **67** 623 (2004)
5. S Grafe *et al*, *J. Raman Spectosc.* **38** 998–1005 (2007)
6. T Brabec and F Krausz *Rev. Mod. Phys.* **72** 545 (2000)
7. C R Calvert, W A Bryan, W R Newell and I D Williams *Phys. Rep.* **491** 1–28 (2010)
8. H Niikura, D M Villeneuve and P B Corkum, *Phys. Rev.* A **73** 021402 (2006), H Niikura, D M Villeneuve and P B Corkum, *Phys. Rev. Lett.* **92** 133002 (2004), H Niikura, P B Corkum and D M Villeneuve, *Phys. Rev. Lett.* **90** 203601 (2003)
9. B Feuerstein and U Thumm, *Phys. Rev.* A **67** 063408 (2003)
10. U Thumm, T Niederhausen and B Feuerstein, *Phys. Rev.* A **77** 063401 (2008), T Niederhausen and U Thumm, *Phys. Rev.* A **77** 013407 (2008)
11. D S Murphy *et al*, *New J. Phys.* **9** 260 (2007), D S Murphy *et al, J. Phys. B: At. Mol. Opt. Phys.* **40** S359–72 (2007), D S Murphy *et al*, *J. Phys.: Conf. Ser.* **58** 371–4 (2007)
12. C R Calvert, T Birkeland, R B King, I D Williams and J F McCann *J. Phys. B: At. Mol. Opt. Phys.* **41** 205504 **(2008)**
13. G L Yudin and M Yu Ivanov, *Phys. Rev.* A **64** 013409 (2001)
14. X M Tong X M, Z X Zhao and C D Lin, *Phys. Rev.* A **66** 033402 (2002)
15. M V Ammosov, N B Delone and V P Krainov, *Sov. Phys.—JETP* **64** 1191 (1986)
16. X Urbain *et al*, *Phys. Rev. Lett.* **92** 163004 (2004)
17. T K Kjeldsen and L B Madsen *Phys. Rev. Lett.* **95** 073004 (2005)

Monochromatic XUV-photon + strong-field NIR cross-correlation by atomic excitation and ionization

Contact *w.a.bryan@swansea.ac.uk*

W A Bryan and G R A J Nemeth
Department of Physics
Swansea University
Singleton Park, Swansea SA2 8PP, UK

F Frassetti, P Villoresi and L Poletto
Laboratory for Ultraviolet and X-rays Optical Research
Department of Information Engineering
via Gradenigo 6/B, 35136 Padova, Italy

R B King and C R Calvert
Department of Pure and Applied Physics
Queen's University Belfast
Belfast BT7 1NN, UK

S G Hook, C A Froud, I C E Turcu and E Springate
Central Laser Facility
STFC Rutherford Appleton Laboratory, Harwell Science and Innovation Campus, Didcot, Oxon OX11 0QX, UK

Introduction

Electronic transitions in matter are responsible for dynamic processes from atomic to macroscopic scales, including the optical properties of materials, chemical bonding and reactivity, conduction, the photoelectric effect and photosynthesis. While electronic transitions can be initiated collisionally, modern physics and chemistry often relies on the absorption of one or more photons over femtosecond to attosecond timescales (10^{-15} to 10^{-18} seconds) to observe such processes. The simplest case is when a single photon is absorbed resonantly. As the photon energy is increased, more tightly bound electrons are accessed, allowing atomic core states to be probed; perturbation theory is generally sufficient to describe such processes. Increasing the photon flux makes the simultaneous absorption of more than one photon likely, resulting in highly nonlinear nonresonant processes which are often described in terms of electronic distortions by the laser-induced electric field; this is generally referred to as the strong-field regime corresponding to an intensity of 10^{13} Wcm^{-2} or higher.

Light source technology defines the parameters which may be explored and controlled. In addition to photon energy and intensity (or flux), key characteristics are bandwidth, duration and repetition rate. Loosely, the photon energy defines the type of transition that can be accessed in a resonant regime or whether transition should be considered as multiphoton or tunnelling in strong-field regime.

Synchrotron radiation, first observed in 1945, is the result of an energetic electron being deflected by a magnetic field, releasing energy in the form of photons. The photon energy is widely tunable by controlling the electron energy, magnetic field strength and bend radius. From the 1960s onwards, massive amounts of information was learnt about electronic processes from tens of eV to hundreds of keV [1]; this continues in Diamond, which produces photons with a high flux and repetition rate, and broad energy tunability. However the photons have poor coherence and pulses tend to be limited to picosecond durations.

The advent of the laser in 1960 saw an alternative method for generating photons which are inherently highly coherent. Advances in technology led first to pulsed operation, followed by broadband amplification techniques that allowed the generation of infrared pulses only a few cycles in duration, hence on femtosecond timescales [2,3,4]. By carefully controlling the temporal and spectral phase of light generated by the oscillator and amplifier, pulses can approach the transform limit. Furthermore, the electric field of these laser pulses is now controllable such that the phase between pulse envelope and carrier oscillation are identical for subsequent pulses. Essentially it is possible to define the group and phase velocities across few hundreds of nanometers of bandwidth. Amplifier technology now means it is possible to generate electric fields of several volts per Angstrom on femtosecond timescales [5]. Modern laser sources are therefore coherent, generate high intensities, are capable of generating ultrashort pulses, however tend not to be tunable and are limited to operate in the IR to UV.

Free-electron lasers (FELs) combine elements of synchrotron and optical laser technology. A relativistic electron beam is passed through a periodic magnetic field in an undulator causing the emission of synchrotron radiation. By employing a series of long undulators FELs can be made to operate in the VUV to x-ray regimes. Such XFELs produce radiation coherent with the electron beam oscillation, causing a temporal bunching and laser gain through self-amplified spontaneous emission (SASE). XFELs such as FLASH in Germany and the LCLS in the US generate a very high intensity over a photon energy range of 10 eV to 1 keV in a pulse tens of femtoseconds long. Noise inherent to the XFEL construction and the SASE process causes a temporal jitter comparable to the pulse duration. While varying the electron beam energy will in principle make the photon energy tunable, in practice XFELs tend to have limitations to their energy flexibility.

High harmonic generation (HHG) in an intense ultrafast laser pulse is an intriguing comprise between an optical and free-electron laser. Following tunnel ionization, the liberated electron propagates in the time-varying laser field, and depending on the instant of release with respect to the laser electric field, can be accelerated back towards the parent ion [6]. Just as with electron impact excitation and ionization experiments, there is a small but measurable likelihood of the electron recolliding with the ion, recombining to a bound state and emitting excess kinetic energy as a photon.

The photon energy, flux and duration emitted during HHG depend on the wavelength, intensity and duration of the optical drive laser field [6]. Furthermore it is vital to observe phase marching conditions between the focus of the laser pulse and the HHG target. Optimal harmonic efficiency is possible by carefully controlling the size of focal volume and number density of the target such that harmonic photons are emitted in as constructively as possible.

By making the drive laser pulse as short as possible [7], typically limited to a few optical cycles, HHG produces an essentially continuous XUV spectrum. By filtering out the lower harmonic orders and minimizing the spectral phase variation over the continuous region, attosecond duration XUV pulses have recently been demonstrated by a number of research groups around the world. Direct observations of electron dynamics are now possible [7]; the majority of experiments have focused on atomic targets. While temporally resolving the electronic motion is a breakthrough, attosecond

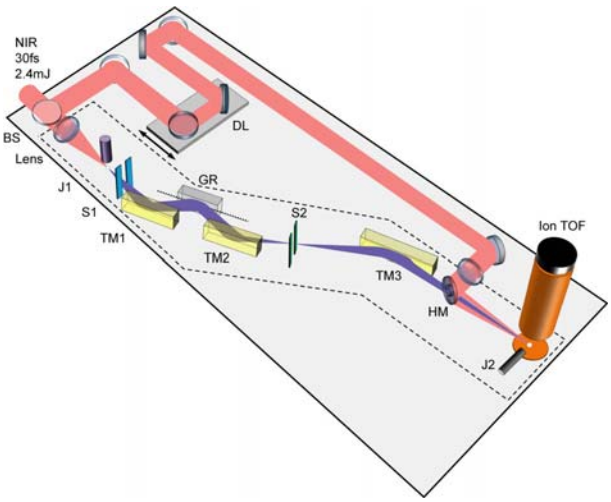

Figure 1. Schematic of XUV beamline including monochromator and NIR delay line. The dashed line indicates UHV chambers, BS – beamsplitter, J1 and J2 – effusive gas jets, TM1-TM3 – toroidal mirrors, GR – grating, S2 – slit, HM – annular mirror.

sources have the disadvantage of requiring a large bandwidth, typically tens of eV at a centre photon energy of ~80 eV, so will excite a broad range of electronic transitions.

HHG driven by an optical laser is the one element of the Artemis Facility and has been demonstrated to generate UV-XUV photons [8]. To make this source more flexible when studying electronic processes, it is now possible to select a single harmonic with an all-reflective monochromator designed and built at LUXOR [9,10,11]. This novel technique combines the femtosecond duration of optical lasers, an energy comparable to attosecond sources while maintaining the narrow bandwidth of XFEL sources, all with an inherent synchronization to a strong-field optical laser pulse. In this commissioning experiment, we intend to demonstrate and measure the temporal duration of the single-harmonic XUV beam by cross-correlating the XUV pulse with an NIR pulse focused to high intensity.

XUV-pump NIR-probe apparatus

The experimental apparatus employed in this work is schematically illustrated in figure 1; the majority of this section of the Artemis beamline has been discussed in recent Annual Report contributions. A 30 fs 4 mJ 800 nm pulse is split 3:1, the weaker beam is transmission focused into an argon gas jet (J1) to an intensity, $I > 10^{13}$ Wcm^{-2}, generating broadband UV-XUV photons up to ~100 eV by HHG [8]. An all-reflective monochromator optimized for the transmission of harmonics 13 to 29 (H13-H29, assuming H1 = 1.56 eV) is used to extract a single harmonic from the XUV region of the spectrum. This monochromator, designed and built by LUXOR, Padova [9,10, 11], consists of a recollimating toroidal mirror, a grating illuminated parallel to the ruling direction, a second toroidal mirror followed finally by a variable width slit in the dispersion plane. By changing the angle of the grating with respect to the incoming XUV beam, the transmitted wavelength is varied and the bandwidth is controlled by changing the slit width.

Following the monochromator, the XUV beam is reflection focused into the interaction region of an ion time-of-flight mass spectrometer (TOFMS) [12]. The focus of the XUV beam is overlapped with a strong-field NIR pulse, generated by transmission focusing the stronger beam from the 3:1 splitter off an annular mirror. Clearly there is a significant energy loss on the annular mirror however the focus at the TOFMS is small enough to produce an intensity in excess of 10^{13} Wcm^{-2}. The relative path length of the NIR and XUV beams is variable

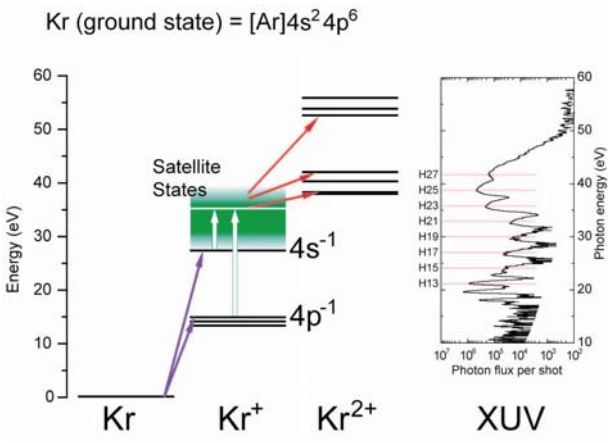

Figure 2. Energy level diagram for krypton showing relevant electronic transitions. The XUV pulse removes a 4s or 4p electron creating Kr^+ (violet arrows), populating highly excited satellite states through shake-up or the configuration interaction (green arrows). The NIR strong field pulse then tunnel ionizes the satellite states (red arrows). The XUV harmonic spectrum is shown (see figure 3).

using a translation stage, which introduce a NIR-XUV delay with a sub-cycle resolution and stability.

Krypton is effusively released into the interaction region of the TOFMS through jet J2. Over the H21-H27 XUV photon range (32.8 – 42.1 eV), krypton will absorb a single photon causing ionization of a 4s or 4p electron with cross sections of 10^{-1} – 10^{-2} or 10^{0} - 10^{1} Mb (1 Mb = 10^{-22} m^2) respectively [13-15]. This leads to the population of highly excited satellite states through shake-up and the configuration interaction [16] as illustrated in figure 2. Now, assuming the NIR pulse arrives after the XUV pulse, the populated satellite states will be readily ionized with near-unity probability, generating Kr^{2+}. However if the NIR pulse precedes the XUV pulse, the NIR intensity is too low to generate significant amounts of Kr^{2+}, so will produce Kr^+ in low-lying electronic states with a probability per NIR pulse of the order 10^{-4} per shot. As a result, the likelihood of the subsequent absorption of an XUV photon is very low. Furthermore, while the XUV photon energy is sufficient to generate Kr^{2+} directly through single-photon double ionization (apparent in figure 2), the cross section is extremely small and indeed only becomes observable with a photon energy in excess of 200 eV or a target pressure approaching 10^{-1} mbar [17].

Characterization of XUV HHG source

To measure the HHG spectrum, a calibrated channel-electron multiplier (CEM) is inserted into the XUV beam after the slit. By recording the CEM output current on an electrometer as a

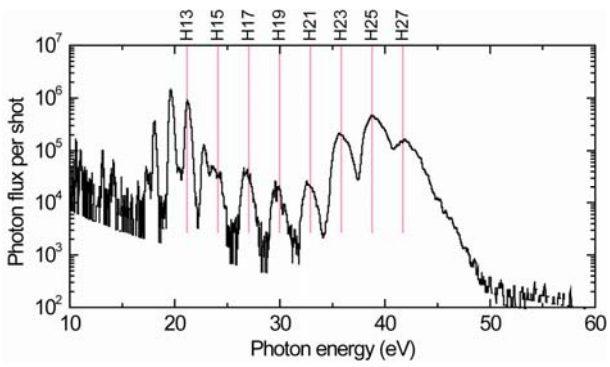

Figure 3. Monochromator transmission as a function of photon energy, corrected for CEM sensitivity (electrons per photon) and dispersion as a function of angle.

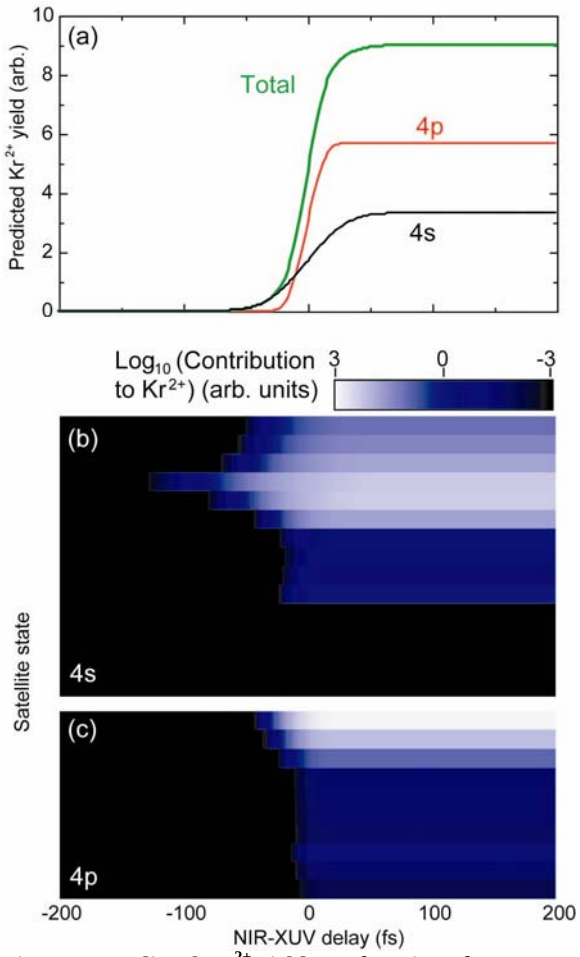

Figure 4. Predicted Kr^{2+} yield as a function of NIR-XUV delay. (a) Total yield along with contributions from ionization of satellite states populated by 4s and 4p ionization. (b) Contribution from individual 4s satellite states as identified in table 1, (c) contribution from 4p.

function of grating angle, the HHG spectrum following the monochromator is measured as presented in figure 3. A number of corrections are applied: the current is converted to number of photons and a Jacobian transform is applied for monochromator transmission as a function of grating angle. Also note the change in harmonic peak width with photon energy which is a consequence of angular dispersion being nonlinear with grating angle. In the present work, we selected a grating optimized to transmit most efficiently between 20-40 eV and at a high resolution, which in this case corresponds to a bandwidth of around 0.7 eV.

Modelling XUV+NIR yield

The duration of the HHG spectrum emitted in J2 (see figure 1), to a reasonable approximation depends on the ionization probability in the 30 fs drive pulse. For a 1.2×10^{13} Wcm^{-2}, 800 nm 30 fs pulse, significant ionization is limited to within a FWHM of 14 fs. This will result in harmonic pulses of FWHM duration between 6 and 9 fs for H21-27. Clearly, the finite size of the illumination spot on the grating and the limited XUV bandwidth will temporally stretch the XUV pulse. To fully quantify this effect, we predicted the amount of Kr^{2+} enhancement depending on the relative delay between the XUV and NIR pulses as a function of XUV photon energy, performing a cross-correlation measurement on the atomic scale. We independently predict the population of the satellite states as a function of time through the XUV pulse according to the pulse intensity and cross section derived from synchrotron measurements [13-15]. Ionization of the satellite states by the strong-field is then modelled using the nonadiabatic theory of

4s satellite states		4p satellite states	
E (eV)	State	E (eV)	State
28.27	$4s^2\ 4p^4\ (^3P)\ 5s$	30.65	$(^3P)5p(^4P_{3/2}) + (^4P_{5/2})$
28.70	$4s^2\ 4p^4\ (^3P)\ 5s$	31.16	$(^3P)5p(^4D_{3/2})$
30.06	$(^3P)4d\ (^4D_{5/2})$	31.22	$(^3P)5p(^2P_{3/2})$
30.23	$(^3P)4d\ (^4P_{1/2}) + (^2P_{1/2})$	31.37	$(^3P)5p(^2P_{3/2})$
32.08	$(^1S)5s(^2S_{1/2})$	31.57	$(^3P)5p(^4D_{3/2})$
33.94	$(^1D)4d(^2S_{1/2})$	31.61	$(^3P)5p(^2D_{3/2})$
34.07	$(^3P)6s(^4P_{1/2}) + (^4P_{3/2})$	31.65	$(^3P)5p(^2S_{1/2})$
34.15	$(^3P)5d(^4D_{1/2})$	32.63	$(^1D)5p(^2P_{3/2})$
34.39	$(^1S)6s(^2S_{1/2})$	34.95	$(^1S)5p(^2P_{3/2})$
36.48	$(^1D)5d(^2S_{1/2})$	35.88	$(^1D)5d(^2G_{9/2})$
37.84	$(^1D)7d(^2S_{1/2})$		
38.99	$(^1D)8d(^2S_{1/2})$		
39.31	$(^1D)9d(^2S_{1/2})$		
39.47	$(^1D)10d(^2S_{3/2})$		

Table 1. 4s and 4p satellite state energies relevant to modelling XUV+NIR cross correlation. Taken from [16].

Yudin and Ivanov [18]. The delay between the XUV and NIR pulses then defines the population of the satellite states that are ionized to Kr^{2+}; the free parameters are then the XUV pulse duration and the intensity of the NIR pulse.

While the cross sections of 4*s* and 4*p* ionization differ by at least an order of magnitude, Calo *et al* [16] have recently observed that the majority of the populated satellite states follow the photon energy dependence of the 4*s* or 4*p* cross sections. We assume their observations apply in the case of HHG XUV photon absorption. The predicted total Kr^{2+} yield is presented in figure 4(a) as a function of NIR-XUV delay for H25 and a NIR peak intensity of 1.2×10^{13} Wcm^{-2}. The different rise times of the 4s and 4p contributions is a result of the relative populations of the satellite states as presented in figure 4(b) and (c), identified in table 1.

Kr^{2+} yield and pulse duration measurement

Before recording the ion yield, the zero delay point has to be identified which could be performed by recording a long delay scan and measuring the Kr^{2+} yield. A much faster alternative is rotating the monochromator grating to allow the zeroth diffraction order to propagate along the beamline; the zero order contains all harmonic orders along with the residual NIR drive radiation. The ZO NIR is synchronized with the XUV pulse, so by interfering the ZO NIR with the NIR reflected from the annular mirror on the exit of the TOFMS, the zero delay time is identified to within an optical cycle.

With the monochromator set to transmit one harmonic, room temperature krypton gas is then effusively released into the interaction region of the TOFMS to a local pressure of ~10^{-4} mbar. Such a high pressure is required as the probability of ionization in either the XUV or NIR pulses is small. Ion time-of-flight spectra are averaged over 2500 laser shots as the NIR-XUV delay is scanned from -200 to 200 fs as presented in figure 5. A least squares fit between the experimentally observed and theoretically predicted Kr^{2+} yield is performed. Note that the model is integrated over the focal volume of the NIR pulse. The best fit is found with a H25 XUV pulse duration of 24 ± 2 fs which is in reasonable agreement with propagating a 8 fs XUV pulse through the monochromator.

Conclusions

By combining high harmonic XUV radiation with a strong-field NIR pulse, single-photon absorption and tunnel ionization have been combined to allow a cross-correlation measurement of the XUV pulse duration. This is made possible by the XUV pulse populating highly excited satellite states in Kr^{+} which are subsequently ionized with a high probability by the NIR pulse. As the delay between the NIR and XUV pulses is scanned, the delay dependent satellite state population regulates the

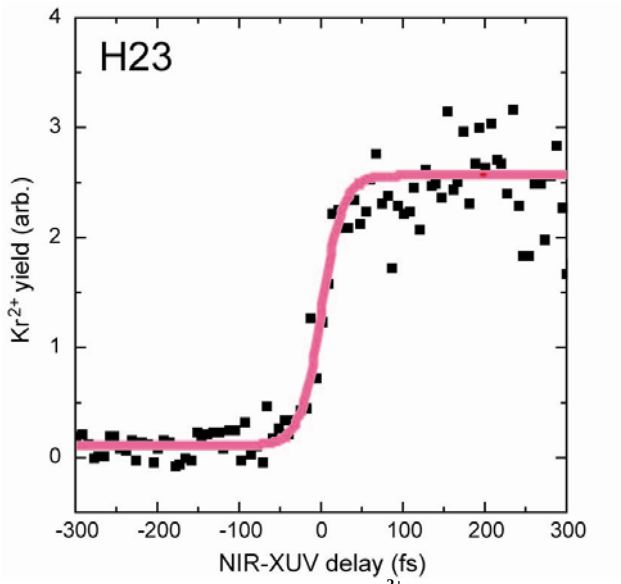

Figure 5. Measured and predicted Kr^{2+} yield as a function of NIR-XUV delay for harmonic 23 (photon energy 35.9 eV, wavelength 34.6 nm). The best least-squares fit reveals the rise of the yield "step" is the result of H23 having a duration of 24 ±2 fs.

measured Kr^{2+} ion yield. This experiment demonstrates that gas-phase atomic and molecular physics can be performed with monochromated XUV radiation from a laser-driven gas source. This technique is highly complementary to HHG attosecond and femtosecond XFEL observations, with inherent sub-femtosecond synchronization to a strong-field NIR pulse and photon energy tunability. The photon flux is the main limitation to this type of measurement, and will be enhanced by at least an order of magnitude by the superposition of non-related frequencies [X] which has the added benefit of more closely spaced harmonic peaks.

Acknowledgements

This work was supported by the Engineering and Physical Sciences Research Council (EPSRC) and the Science and Technology Facilities Council (STFC), UK. CRC and RBK acknowledge financial support from the Department of Education and Learning, Northern Ireland; GRAJN acknowledges financial support from EPSRC and STFC.

References

1. V Schmidt, *Electron Spectrometry of Atoms Using Synchrotron Radiation* (Cambridge University Press, Cambridge, England 1997)
2. S. Backus *et al. Rev. Sci. Instrum.* **69** 1207 (1998)
3. D. H. Sutter *et al*, Opt. Lett. **24** 631 (1999)
4. U. Morgner *et al*, Opt. Lett. **24** 411 (1999)
5. T Brabec and F Krausz, *Rev. Mod. Phys.* **72** 545 (2000)
6. P Agostini and L F DiMauro, *Rep. Prog. Phys.* **67** 813 (2004)
7. F Krausz and M Ivanov, *Rev. Mod. Phys.* **81** 163 (2009)
8. I C E Turcu *et al*, *SPIE Proc.* **7467** 746902 (2009)
9. P. Villoresi, Appl. Opt. **38**, 6040 (1999).
10. L. Poletto, Appl. Phys. B **78**, 1013 (2004)
11. L Poletto *et al*, *Opt. Lett.* **32** 2897 (2007)
12. W A Bryan *et al*¸*Nat. Phys.* **2**, 379 - 383 (2006)
13. U Becker and D A Shirley, *VUV and Soft X-ray Photoionization* (Plenum Press, New York, 1996)
14. H Yoshii *et al*, *J. Electon Spectrosc. Relat. Phenom.* **144-147** 83 (1994)
15. A Kikas *et al*, *J. Electon Spectrosc. Relat. Phenom.* **77** 241 (1996)
16. A Calo *et al*, *J. Phys. B* **39** 4169 (2006)
17. J H D Eland *et al*, *Phys. Rev. Lett.* **90** 053003 (2003)
18. G L Yudin and M Yu Ivanov, *Phys. Rev. A* **64** 013409 (2001).

Multi-pulse scheme for controlling electron localisation upon molecular dissociation

Contact *rking05@qub.ac.uk, c.calvert@qub.ac.uk*

R. B. King, C. R. Calvert, J. D. Alexander, L. Belshaw, J. F. McCann, J. B. Greenwood and I. D. Williams

School of Mathematics and Physics, Queen's University Belfast, University Road, Belfast, BT7 1NN, UK

W. R. Newell

Department of Physics and Astronomy, University College London, Gower Street, London, WC1E 6BT, UK

W. A. Bryan

Department of Physics, Swansea University, Singleton Park, Swansea, SA2 8PP, UK

Introduction

Intense ultrashort pulses produced from titanium sapphire (Ti:sapph) laser systems provide powerful tools for probing and controlling molecular dynamics. With each technological development, new applications are found for these highly versatile systems. We propose a new application of this technology in quantum control of electron dynamics.

A significant development in this ultrashort pulse technology has arisen via spectral broadening techniques (such as self-phase modulation [1] and filamentation [2]), where it is now possible to generate pulses with durations on the order of a few cycles of the carrier field (where 1 cycle = 2.66 femtoseconds for 800 nm). High-impact applications of such pulses have been found in the production of XUV pulses via high harmonics [3, 4], the generation of attosecond pulses [5] and the probing of molecular motion [6-10].

For such short pulse durations, the position of the electric field oscillation relative to the pulse envelope becomes extremely important. This is appropriately quantified as the carrier-envelope-phase (CEP) offset, φ, as indicated in the pulse profile shown in Figure 1 (a). For ultrafast experimental applications, it is extremely advantageous to be able to fix this CEP, now possible through stabilisation loops [11].

An exciting application of CEP-fixed few-cycle pulses is in the quantum control of molecules. In this report we describe a new, multi-pulse scheme to achieve and enhance electron localisation upon dissociation, using bound vibrational wavepacket dynamics. Using recent theoretical results [12] we will show that this scheme not only utilises an alternative mechanism to other techniques [13, 14], but can also lead to significant enhancement in localisation via manipulation of the bound wavepacket.

Electron Localisation in D_2^+

The hydrogen molecular ion is an ideal candidate when studying fundamental dynamics in intense fields. As a three-body problem it is theoretically tractable, especially when treated within the Born-Oppenheimer and dipole approximations. The larger reduced mass of the deuterium molecular ion makes it more suitable for experimental studies of wavepacket dynamics with ultrashort laser pulses, having vibrational periods of the order of 20 fs.

When intense (up to 4×10^{14} Wcm^{-2}) near-infrared laser pulses interact with the deuterium molecular ion, only two electronic states are significantly coupled and need to be considered when treating the resulting dynamics.

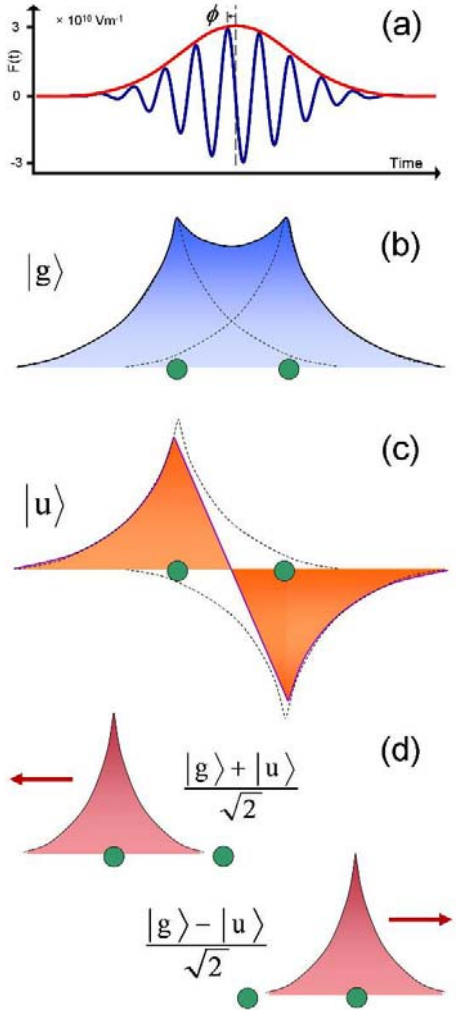

Figure 1. (a) Sketch of the Electric field for a CEP stabilised pulse where the CEP offset has been set to $\pi/2$. (b) and (c) Schematics of the electron orbitals for the two lowest lying states of D_2^+, $1s\sigma_g$ (|g›) and $2p\sigma_u$ (|u›). (d) How electron localisation can be determined if dissociation occurs via a superposition of the two electronic states for a particular R value.

As sketched in figure 1 (b) the wavefunction of the lowest energetic state (|g›) corresponds to a high probability of the electron being located between the two deuterons, creating a bound state. The second accessible state (|u›) has an equal probability of the electron localising to either nucleus, and is a dissociative state. If dissociation occurs via one of these two

states, the electron has equal probability of being bound to one nucleus or the other.

However, if a nuclear wavepacket can be manipulated to dissociate via both these channels simultaneously, (i.e. in a superposition of the two electronic states) then it becomes possible to determine which nucleus the electron localises to; examples of this are shaded in red in figure 1 (d).

Figure 1 displays how the wavefunctions of the electronic states can be rewritten into a new basis set where it is possible to determine which of the nuclei the electron will localise to should photodissociation occur via both states. As described by Kling *et al.* [kling] the new nuclear wavefunctions can be expressed as:

$$\phi_l(R,t) = \frac{\phi_g(R,t) + \phi_u(R,t)}{\sqrt{2}}$$

$$\phi_r(R,t) = \frac{\phi_g(R,t) - \phi_u(R,t)}{\sqrt{2}} \qquad [1]$$

Where φ_g and φ_u are the dissociating nuclear wavefunctions on the $1s\sigma_g$ and $2p\sigma_u$ states respectively. We can then define an absolute asymmetry parameter for the localisation as

$$A = \int |\phi_l(R,t)|^2 \, dR - \int |\phi_r(R,t)|^2 \, dR \qquad [2]$$

It is worth noting that dissociation does not occur after every pulse interaction, and this point is implicit in the above definition. Elsewhere [13, 14] a normalised asymmetry parameter is used, where the asymmetry is expressed as a percentage of the probability of dissociation. However this can be misleading as it may infer a large asymmetry in cases where the actual probability of dissociation is low. In the work discussed here, we place an emphasis on achieving large asymmetry *and* significant dissociation probability.

The Multi-pulse Scheme

It follows from Equation (1), that the requirement for controlling electron localisation upon dissociation is to ensure that fragmentation of the molecule occurs in a superposition of the two electronic states. Our scheme is to launch a bound vibrational wavepacket in D_2^+ and, via manipulation of this wavepacket, to guide the molecule towards dissociation on both electronic surfaces, thus leading to electron localisation. This is done via a multi-pulse scheme, as sketched in Figure 2.

- First, a pump pulse (pulse 1) ionises the neutral deuterium molecule creating a vibrational wavepacket in the $1s\sigma_g$ ground electronic state of the deuterium molecular ion [6, 7, 8].
- A second time-delayed pulse (pulse 2) is applied to modify the vibrational wavepacket, redistributing the vibrational population [15, 16] and thus, inherently manipulating the wavepacket dynamics.
- The third pulse guides the modified wavepacket towards dissociation, localising the electron to one nucleus or t'other.

The timing of both the second and third pulse interactions are set to coincide within a time window where the nuclear wavepacket is oscillating in a well localised manner i.e. during a vibrational revival.

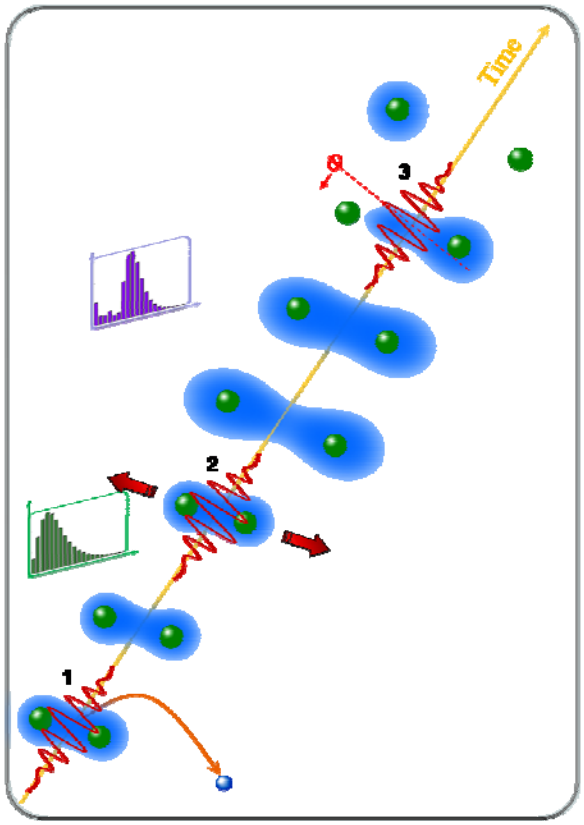

Figure 2. Multi-pulse scheme for enforcing electron localisation. Pulse 1 ionises the neutral D_2 molecule creating a vibrational distribution (green bar chart) in D_2^+, pulse 2 is used to cause vibrational heating within the molecule (purple bar chart). This is subsequently fragmented via pulse 3, where tuning of its CEP controls which nuclei the electron localises to.

The control and dissociation dynamics are simulated using a quantum model which is well-established for vibrational wavepacket dynamics in D_2^+ [15]. The pump process is assumed to project the ground state wavefunction (v=0) of the neutral onto the ground electronic surface of the molecular ion. The resulting wavepacket is propagated within the time-dependent Schrodinger equation, via a Taylor expansion of the time-evolution operator. Subsequent pulse interactions with the vibrational wavepacket are incorporated in the Hamiltonian, expressed as a coupling between the two electronic states.

The characteristics of the control and dissociation pulses (7 fs FWHM duration, 2×10^{14} Wcm^{-2} intensity) were chosen to reflect typical outputs from ultrashort pulse generation techniques, as well as to limit the onset of further ionisation [17], and were delayed with respect to the initial pump interaction over a range of delays in order to find the optimal conditions for electron localisation.

Results

Figure 3 displays results for optimised 2-pulse (b) and 3-pulse (d) simulations as a function of pulse CEP (φ), with the asymmetry summed over all dissociation events. There is a clear sinusoidal oscillation of the asymmetry as a function of φ. In the 2-pulse case a maximum asymmetry of 0.22 is achieved corresponding to a left: right ratio of just over 5:2. With the modified vibrational distribution fig 3(c) the asymmetry parameter reaches a maximum of 0.42 which equates to a left: right ratio of 4:1 and implies that the final position of the electron can be steered to the left in up to 80 % of the dissociation events during this pulse interaction.

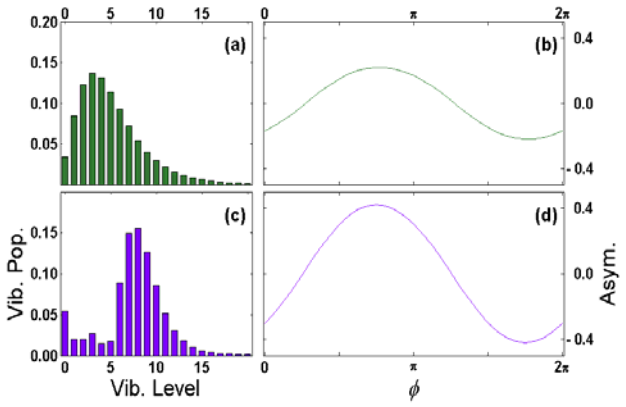

Figure 3. Asymmetry results for dissociation of a D_2^+ vibrational wavepacket. (a) Vibrational distribution created by the pump pulse. (b) Asymmetry as a function of CEP (φ) for dissociation of the distribution in (a), i.e. no control pulse applied. (c) Modified vibrational distribution created by a control pulse interaction at 598 fs. (d) Asymmetry for the modified vibrational wavepacket. For both (b) and (d) the timing of the dissociation pulse has been optimally chosen to enhance the dissociation probability and asymmetry.

In an experiment using apparatus such as a time of flight mass spectrometer [7, 8] or cold-target recoil-ion momentum spectroscopy device [9, 13] ions can be detected as a function of their kinetic energy release, constituting a key experimental observable. This can also be calculated from our results making it possible to observe how the asymmetry parameter varies as a function of the deuteron energy.

The kinetic energy release is shown in Figure 4 as a function of phase, for the optimised 3-pulse scenario where the colour scale denotes the strength of the asymmetry (red indicating the electron predominantly localising to the left nucleus and the blue indicating that is localises to the right). The figure indicates that controlled asymmetry is more likely to occur within certain energy ranges so while in this case the *total asymmetry* ratio is 4:1, within the energy range of 0.2 – 0.4 eV a peak ratio of 11:1 is observed meaning that 92% of the dissociation events that occur within this energy range can be manipulated by the pulse CEP. This is a significant enhancement on any previously observed asymmetry values.

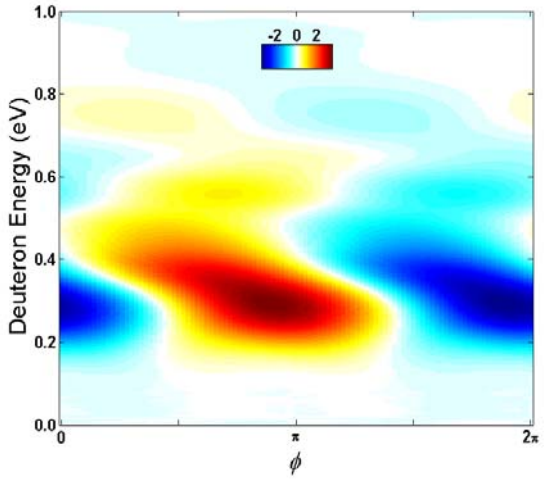

Figure 4. Electron asymmetry as a function of the dissociating pulse's CEP (φ) and kinetic energy of the dissociating deuterons. Colour scale denotes localisation where red = left nucleus and blue = right nucleus.

Conclusions

With current ultrashort laser technology, it is clear that we can turn our attention to the goal of controlling the motion of electrons in dissociating molecules. Before this is attempted in large molecules, it is useful to demonstrate the principle in simpler prototypal systems. Using established theoretical simulations we have identified an experimental configuration which uses the motion of a vibrational wavepacket and the pulse CEP to gate the electron localisation during photodissociation. By modifying the vibrational motion of the molecule, we can prepare the target into a suitable configuration for significant control to be exerted over the electron's final position. The localisation of the electron can be increased to 80% in all dissociation events and up to 92% within a 0.2 eV energy range.

Acknowledgements

R B King acknowledges funding from the Department for Employment and Learning (NI). J D Alexander acknowledges funding from the European Social Fund. C R Calvert acknowledges funding from the Leverhulme trust.

References

1. Stolen R H and Lin C, *Phys. Rev.* A **17** 1448 (1978)
2. Hauri C P, Kornelis W, Helbing F W, Heinrich A, Couairon A, Mysyrowicz A, Biegert J and Keller U, *Appl. Phys. B* **79** 673 (2004)
3. Haworth C A, Chipperfield L E, Robinson J S, Knight P L, Marangos J P, Tisch J W G, *Nature Physics* **3** 52 (2007)
4. Turcu I C E *et al., Proc. SPIE Vol.* **7469** 746902 (2010)
5. Goulielmakis E *et al.*, *Science* **320** 1614 (2008)
6. Calvert C R, Bryan W A, Newell W R, Williams I D, *Physics Reports* **491** 1 (2010)
7. Bryan W A *et al.*, *Phys. Rev. A* **76** 053402 (2007)
8. McKenna J *et al.*, *J. Mod. Opt.* **54** 1127 (2007)
9. Ergler Th, Rudenko A, Feurstein B, Zrost K, Schröter C D, Moshammer R, Ullrich J, *Phys. Rev. Lett.* 97 193001 (2006)
10. Baker S, Robinson J S, Haworth C A, Teng H, Smith R A, Chirilă C C, Lein M, Tisch J W G, Marangos J P, *Science* **312** 424 (2006)
11. Baltuška A, Uiberacker M, Goulielmakis E, Kienberger R, Yakovlev V S, Udem T, Hänsch T W, Krausz F IEEE J. Sel. Top. Quantum Electron **9** 972 (2003)
12. Calvert C R, King R B, Bryan W A, Newell W R, McCann J F, Greenwood J B and Williams I D, *J. Phys. B* **43** 011001 (2010)
13. Kling M F, Siedschlag Ch, Verhoef A J, Khan J I, Schultze M, Uphues Th, Ni Y, Uiberacker M, Drescher M, Krausz F, Vrakking M J J, *Science* **312** 246 (2006)
14. He F, Ruiz C, Becker A, *Phys. Rev. Lett.* **99** 8 (2007)
15. Calvert C R, Birkeland T, King R B, Williams I D and McCann J F, *J. Phys. B* **41** 205504 (2008)
16. King R B *et al.*, CLF Annual report p82 (2007/08)
17. Roudnev V and Esry B D, *Phys. Rev. A* **76** 023403 (2007)

Intensity-resolved ionization processes in few-cycle strong-field laser pulses

Contact *g.r.a.j.nemeth.290703@swan.ac.uk*

G. R. A. J. Nemeth and W. A. Bryan

Department of Physics, Swansea University, Singleton Park, Swansea, SA2 8PP, UK

R. B. King, J. D. Alexander, C. R. Calvert, J. B. Greenwood and I. D. Williams

School of Mathematics and Physics, Queen's University Belfast, University Road, Belfast, BT7 1NN, UK

W. R. Newell

Department of Physics and Astronomy, University College London, Gower Street, London, WC1E 6BT, UK

S. Hook, C. A. Froud, I. C. E. Turcu and E. Springate

Central Laser Facility, STFC Rutherford Appleton Laboratory, Didcot, Oxon OX11 0QX, UK

Introduction

In an intense laser field, ionization of atoms or molecules can proceed via the absorption of one or more photons, or by tunnelling due to distortion of the Coulomb potential by the incident electric field, as reviewed in[1]. In this work, the authors concentrate on tunnel ionization only, as this is expected to be the dominant ionization process in few-cycle near-infrared (NIR) strong-field laser pulses. Keldysh[2] was the first to attempt to quantify tunnelling, and his work has inspired several developments to the theory in the past fifty years[3,4,5,6]. Most assume the outgoing electron can be considered separately to the parent ion after ionization, influenced only by the oscillating laser field. Corkum successfully explained non-sequential ionization processes such as recollision[7] by treating the electron in this manner. Recollision occurs when in a linearly-polarized field the outgoing electron is accelerated back towards the parent ion within the same laser period which caused the initial ionization. The returning electron recombines with the parent ion or causes the removal of another electron. However, when these effects are suppressed, such as in the case of circularly-polarized pulses which send the outgoing electron on a trajectory which makes it unlikely to return to the parent ion, differences between theory and experiment are still seen. These differences have previously been attributed to excitation due to 'shake-up' by Bryan *et al.*[8]. Due to the violent removal of the electron during an intense few-cycle pulse, higher-energy states with the same electron configuration can be populated. Alternatively, the population of higher-energy states could be explained by tunnel ionization directly to those states. It is also possible that lower-lying orbitals are involved in tunnelling, which have a much smaller but non-negligible ionization probability. Tunnel ionization from an orbital (HOMO-1) below the highest occupied molecular orbital (HOMO) has recently been experimentally observed in molecules by Akagi *et al.*[9]. The ability to distinguish the orbital from which the electron has been ejected opens up the possibility of probing attosecond dynamics of individual electron orbitals.

A complete understanding of the tunnel ionization step is central to being able to control processes such as recollision, which is the first step in the production of attosecond extreme-ultraviolet (XUV) pulses by high-harmonic generation (HHG)[7], tomographic reconstruction of electron orbitals[10], and is used as the electronic 'probe' step in overlapped XUV-NIR experiments[11,12]. There are also implications for molecular studies which use strong-field ultrashort pulses to initiate photodissociation and/or Coulomb explosion by ionization. An example would be the study and control of vibrational wavepackets, recently reviewed by Calvert *et al.*[13].

We investigate tunnel ionization in xenon atoms using a few-cycle (~10 fs) NIR (700 – 900 nm), intense (10^{13} – 10^{15} W/cm^2) laser pulse generated at Artemis using a hollow-fibre compressor[14], which is temporally and spectrally characterized using frequency-resolved optical gating (FROG)[15]. The pulse is circularly polarized to suppress recollision effects. The ionization yield is measured with respect to distance from the focus, which will allow the yield to be intensity resolved. The results are compared to tunnelling models based on the theory of Yudin and Ivanov[5], a popular theory in the attosecond community and is applicable to arbitrary values of the Keldysh parameter γ[2]. The proposed models take into account ionization between all possible combinations of inner- (5*s*) and outer-valence (5*p*) electron energy levels, and can be compared to ground-state only calculations to highlight the importance of their inclusion.

Eventually, the deconvolution method originally proposed by Van Woerkum *et al.*[16,17] and further developed by Bryan *et al.*[18] for a non-Gaussian focus will be used to extract ionization probabilities from the intensity-resolved experimental data, the results of which can be compared directly to calculated ionization probabilities. The deconvolution procedure relies on the correct characterization of the focal region. The laser focus is simulated by propagating an input beam profile through an ABCD system matrix. The input profile can be assumed to be Gaussian at the output of a typical laser resonator, but in the case of hollow-fibre compression is expected to be Bessel[19]. Diffraction due to truncation would affect both beam profiles, but in the case of a truncated Bessel non-trivial focal distributions are anticipated[20].

Modelling tunnel ionization

Bryan *et al.*[8] demonstrated the importance of considering multiple electron energy levels in Ar tunnel ionization, finding better agreement between theory and experiment when multiple levels were included in the models used. The difference between multiple-energy-level and ground-state-only ionization was attributed to excitation caused by the outgoing electron, populating higher-energy ionic energy states. Recently, Akagi *et al.*[9] identified ionization directly from a lower-lying molecular orbital (HOMO-1) in HCl due to tunnelling, with a lower but significant probability than the highest-occupied molecular orbital (HOMO). The HCl energy levels identified are of similar order to those in xenon, and their experiment uses similar laser intensities to the authors' experiment.

Ionization probability strongly depends on the Keldysh parameter γ, which depends on the duration and intensity of the laser pulse, as well as the ionization potential I_p. For the removal of lower-lying electrons, I_p is much larger (in xenon, 23.4 eV for 5*s* removal, compared to 12.1 eV for ground-state 5*p* removal), and therefore the ionization probability is smaller, but not negligible. It may be possible for electrons to directly tunnel from lower-lying orbitals, leaving the ion in a higher-energy electron configuration. There are also multiple energy levels for each electron configuration (for Xe^{2+}, there are five $5p^{-2}$ levels in the range 33.1 – 37.6 eV[21]) which are neglected when considering only ground-state ionization, tunnelling to each of which may contribute to the total ionization probability.

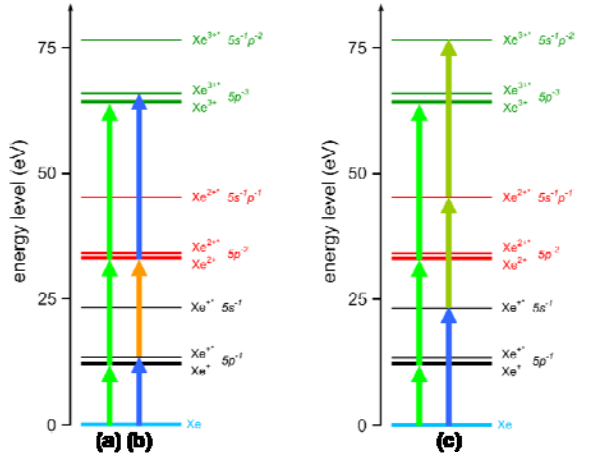

Figure 1: *Valence energy levels in xenon, with example ionization pathways: (a) the outermost 5p electron is removed, creating ions in the ground state; (b) a lower-lying 5p electron is removed from the neutral atom to create an Xe^+ ion with a higher-energy electron configuration, which requires less energy to ionize further to Xe^{2+}; (c) an inner-valence 5s electron is removed from the neutral atom with a much lower probability in Xe^+, but ionization proceeds in subsequent charge states by 5p-electron removal, therefore contributing to the ionization*

Figure 1 pictorially represents the effect of including multiple energy levels on the number and nature of the ionization pathways. Any differences in ionization probability with respect to ground-state ionization are expected to be small for Xe^+, and increase with each subsequent charge state due to the increase in the number of available energy levels.

Ionization is modelled using the tunnelling rates calculated using the theory of Yudin and Ivanov[5]. The resulting ionization probabilities are shown in Figure 2, which shows ground-state only and multiple 5*p*- and 5*s*-level ionization. Allowing tunnelling from the ground-state and next-lowest-lying 5*p* state introduces a small shift in the ionization probability. However, it can be seen that allowing for the cumulative effect of ionization from all 5*p*- and 5*s*-levels results in a substantial shift in ionization probability to lower intensities. The model takes into account ionization from all possible combinations of levels, hence the probability shifts become larger with increasing charge state.

Experimental setup

Figure 3 shows the layout of the experiment. A Femtolasers CompactPro Ti:S laser system produces 1 mJ, 30 fs NIR pulses which are spectrally broadened by self-phase modulation in an argon-filled hollow fibre[19], and recompressed to ~10 fs by a series of chirped mirrors which compensate for the group-delay dispersion acquired after propagation through the fibre. A quarter-wave plate converts the pulse from linear to circular polarization. The pulse is reflectively focused (f = 50 mm) into an effusive xenon gas jet, generating intensities of 10^{13} – 10^{15} W/cm^2 over the focal region. The ions produced are detected using an ion time-of-flight (TOF) mass spectrometer, with a 250 µm aperture to limit the z-range, and therefore the range of intensities over which the ions are detected. The focusing mirror is varied with 100 µm resolution, translating the laser focus with respect to the aperture in the TOF. As a result, z-scans of ion yield vs. mirror position can be produced.

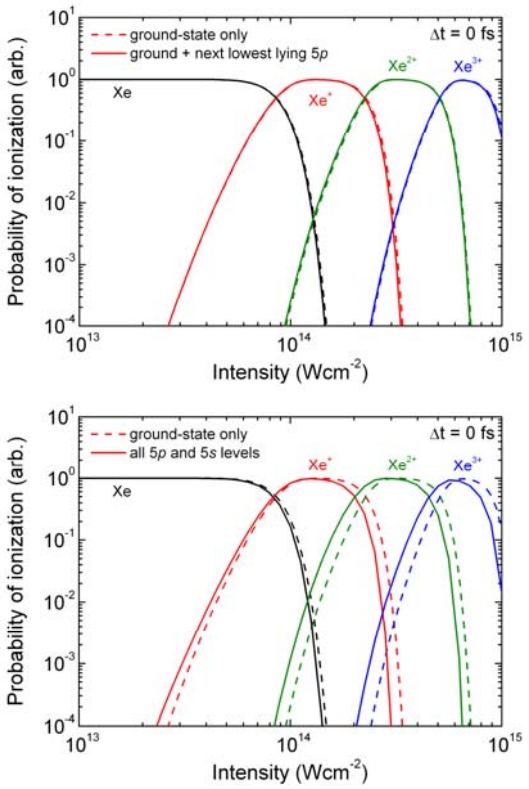

Figure 2: *Predicted ionization probabilities from the theory of Yudin and Ivanov; (top) ground-state only ionization (dashed line) and ionization from the ground-state and next-lowest-lying 5p state only (solid line); (bottom) ground-state only ionization (dashed line) and ionization from all 5p and 5s states (solid line).*

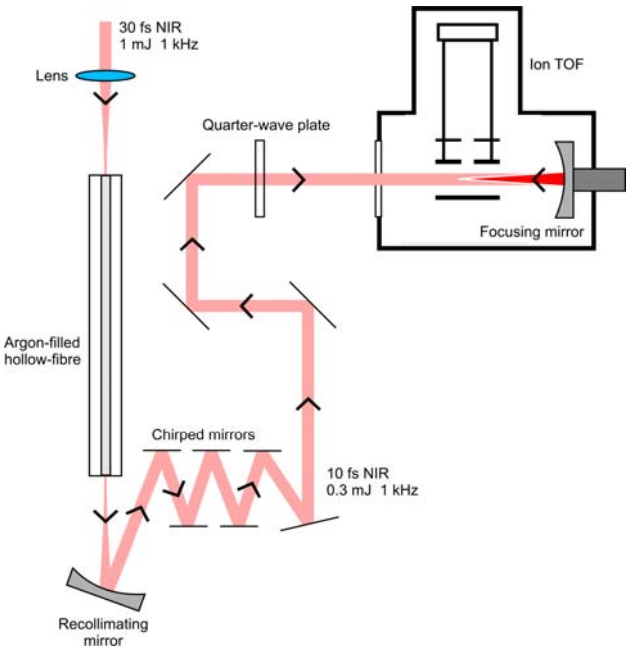

Figure 3: *Experimental setup for temporally-shaped ultrashort NIR pulses. An argon-filled hollow fibre and chirped mirrors compress the initially 30 fs pulse to ~10 fs. The focusing mirror can be translated with respect to the TOF to spatially resolve ion production over the focal region. An effusive xenon gas jet (not shown) is situated near the focus.*

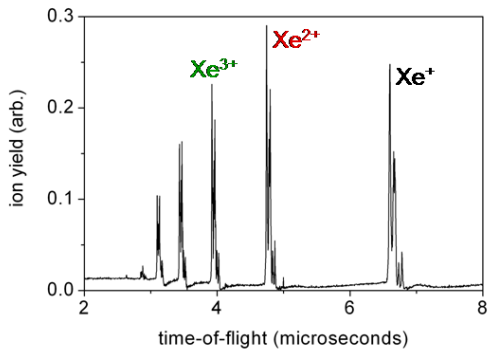

Figure 4: *Xenon ion TOF spectrum, with the first three charge states identified.*

Results

The xenon TOF spectra, an example of which can be seen in Figure 4, consist of ion yields for Xe^{+} to Xe^{8+} separated due to their charge-to-mass ratio. TOF spectra are recorded for a range of distances from the focus, *z*. The ion yields for each charge state can be integrated, and plotted with respect to distance from the focus, producing *z*-scans. For successive charge states, the atomic ion requires higher intensities to ionize further, corresponding to a decrease in the signal-producing volume. This can be seen in the *z*-scans shown in Figure 5. Saturation behaviour is seen in the ion yields, most prominently in Xe^{+}, where the yield depletes due to the probability of ionization in the next-highest charge state becoming significant.

The deconvolution[18] procedure to extract ionization probabilities directly from *z*-scans is outlined in Figure 6. The on-axis intensity distribution is simulated over the same distance range as the *z*-scans by propagating an input beam through an ABCD optical system matrix representing the actual experimental setup in Figure 3. The deconvolution routine takes the on-axis intensity and integrated ion yield as inputs, and produces an ionization probability. The beam width and divergence at the input is not known precisely, and becomes the fitting parameter which is varied until good agreement is found between the theory and the deconvoluted ionization probabilities for the lowest charge state (Xe^{+}), which should be least affected by any excitation processes.

In order to verify the correct working of the deconvolution procedure, a three-dimensional ion-signal-producing volume has been simulated assuming a Gaussian intensity distribution at the input to the optical system matrix, with the parameters adjusted so that the features are on a similar scale to those of the experiment. Simulated *z*-scans were produced by integrating over a cylinder (250 μm radius) of the simulated volume over the same range of *z* used in the experiment, echoing the way in

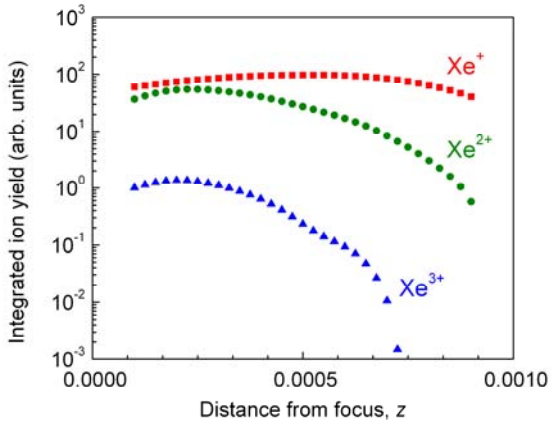

Figure 5: *Experimental z-scans of integrated ion yield with respect to distance from the focus.*

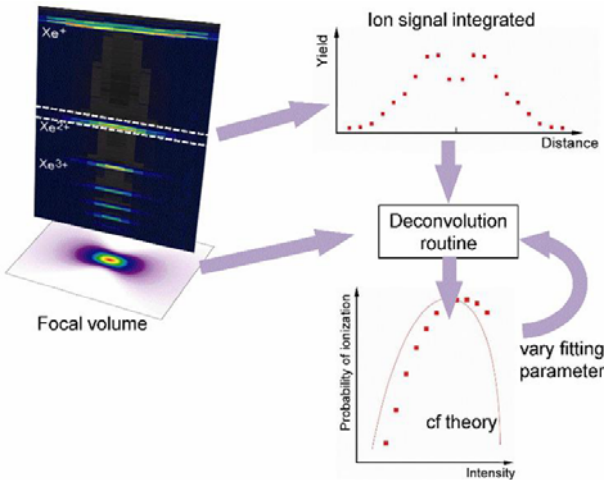

Figure 6: *Deconvolution procedure to extract ionization probabilities from experimental z-scans.*

which the ion yield is recorded by the apertured TOF. Since the simulated ion yields follow the predicted ionization probabilities for multiple electron levels as shown in Figure 2 (multiple 5*p* and 5*s* ionization), deconvoluting the simulated *z*-scans with respect to the simulated on-axis intensity distribution is expected to reproduce these probabilities, the results of which are shown in Figure 7. Apart from slight variations attributed to quantization of the signal volume in the simulation, the original input ionization probabilities are reproduced by the deconvolution.

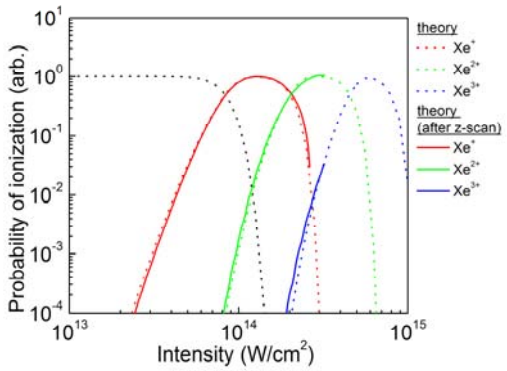

Figure 7: *Predicted ionization probability before (dashed lines) and after (solid lines) being extracted from a simulated three-dimensional Gaussian ion-producing volume by deconvolution.*

Conclusions

The recollision-free ionization of xenon in a NIR strong-field few-cycle laser pulse has been measured experimentally. Numerical models have been developed to take into account the contribution of multiple energy levels to the total tunnel ionization probability. The deconvolution procedure has been tested for a Gaussian input profile. Full characterization of the laser focus for a Bessel input profile is underway. The experimental ionization probabilities will be extracted from the data using the deconvolution method described earlier, the results of which will be the subject of a forthcoming publication.

Acknowledgements

G. R. A. J. Nemeth would like to acknowledge funding from EPSRC and STFC. R. B. King and C. R. Calvert would like to acknowledge funding from the Department of Education and Learning (Northern Ireland). J. D. Alexander would like to acknowledge funding from the European Social Fund.

References

1. A. Scrinzi *et al.*, J. Phys. B: At. Mol. Opt. Phys. **39** R1-R37 (2006).
2. L. V. Keldysh, Sov. Phys. JETP **20**, 1307 (1965).
3. M. V. Ammosov, N. B. Delone, and V. P. Kraĭnov, Sov. Phys. JETP **64**, 1191 (1986).
4. A. M. Perelomov, V.S. Popov, and M. V. Terent'ev, Sov. Phys. JETP **23**, 924 (1965).
5. G. L. Yudin and M. Y. Ivanov, Phys. Rev. A **64**, 013409 (2001).
6. A. Becker and F. H. M. Faisal, J. Phys. B: At. Mol. Opt. Phys. **38** R1-R56 (2005).
7. P. B. Corkum, Phys. Rev. Lett. **71**, 1994-1997 (1993).
8. W. A. Bryan *et al.*, Nat. Phys. **2**, 379-383 (2006).
9. H. Akagi *et al.*, Science **325**, 1364 (2009).
10. O. Smirnova *et al.*, Nature **460**, 972-977 (2009).
11. M. Uiberacker *et al.*, Nature **446**, 627-632 (2007).
12. W. A. Bryan *et al.*, CLF Annual Report (2009-2010).
13. C. R. Calvert, W. A. Bryan, W. R. Newell and I. D. Williams, Phys. Rep. **491**, 1-28 (2010).
14. I. C. E. Turcu *et al.*, Proc. SPIE **7469**, 746902 (2009).
15. D. Kane and R. Trebino, IEEE J. Quantum Electron. **29** 571 (1993).
16. M. A. Walker, P. Hansch and L. D. Van Woerkum, Phys. Rev. A **57** R701 (1998).
17. P. Hansch, M. A. Walker and L. D. Van Woerkum, Phys. Rev. A **54** R2559 (1996).
18. W. A. Bryan *et al.*, Phys. Rev. A **73**, 013407 (2006).
19. M. Nisoli *et al.*, Opt. Lett. **22**, 8 (1997).
20. S. De Nicola, Pure Appl. Opt. **5**, 827-831 (1996).
21. E. B. Saloman, J. Phys. Chem. Ref. Data **33**, 765 (2004).

Ultrafast dynamics of electronic structure in complex materials

Contact *j.petersen1@physics.ox.ac.uk*

J.C. Petersen[*], **N. Dean**
Clarendon Laboratory, Oxford University

S. Kaiser, A. Cavalieri, A. Cavalleri[†]
Max Planck Department for Structural Dynamics, Centre for Free-Electron Laser Science, University of Hamburg, Germany

[*]*Also at MPSD, CFEL, Hamburg*
[†]*Also at Clarendon Laboratory, Oxford University*

C. Cacho, E. Springate, E. Turcu
Central Laser Facility, STFC Rutherford Appleton Laboratory

S. Dhesi
Diamond Light Source

H. Berger
EPFL, Lausanne, Switzerland

Introduction

A fascinating variety of ordered phases emerge in systems with large, direct correlations between individual electrons [1], but their inherent complexity and the fact that diverse interactions take place on similar energy scales mean that a great deal of experimental input is often necessary. Invaluable techniques have included Angle-Resolved Photoemission Spectroscopy (ARPES), which maps out electronic band structure as a function of energy and momentum [2], and pump-probe studies, in which a transient excited state is produced by a femtosecond laser pulse and then studied by a second pulse after some delay [3]. Recently these techniques were combined to study the electronic structure of a transient phase using ultrashort UV pulses [4]. The new materials science beamline at Artemis has been commissioned to carry out this type of experiment. By employing high-harmonic pulses to generate photoelectrons, it offers the possibility of measuring time-resolved photoelectron spectra at momenta across the entire Brioullin zone. The test case for this new apparatus has been the layered sulphide 1T-TaS_2, which exhibits a range of phenomena of current interest.

1T-TaS_2

When cooled, this material undergoes a series of phase transitions as long-wavelength modulations in charge density form within the two-dimensional layers that make up its structure. At 180 K the Charge Density Wave (CDW) becomes commensurate and 'locked in' to the lattice, producing a static distortion to the charge density and atomic positions. The Ta ions form star-shaped clusters of 13 ions each. The resulting change in electronic structure removes 12 out of 13 electrons from the conduction band [5]. Cluster formation also increases the Coulomb interaction between remaining conduction-band electrons, causing localization and the opening of a Mott gap. Photoexcitation can destroy the Mott order and simultaneously excite an amplitude mode of the CDW. Optical measurements of the transient phase [6] reveal the combined effect of these processes. Time-resolved ARPES measurements at 6 eV showed a reduction of spectral intensity in the Lower Hubbard band (LHB) at the zone centre (k=0), corresponding to collapse of the Mott gap, followed by oscillation in the position of the band edge due to the CDW amplitude mode [4].

TR-ARPES on TaS_2 at Artemis

The measurements we show here are angle-integrated to include contributions from the entire folded Brioullin zone. Fig. 1 shows a map of photoelectron intensity as a function of energy and time. Immediately after photoexcitation with a 30 fs pulse of 1.5 eV light there is a collapse in intensity in the LHB, transfer of spectral weight towards the Fermi level, and subsequent oscillation of the LHB profile at the frequency of the CDW amplitude mode. These features agree well with those seen at k=0 [4], but our angle-integrated measurements additionally show an oscillation in the LHB peak intensity (Fig. 2), a new effect which we tentatively attribute to the influence of the CDW amplitude mode on the peak density of states for momenta near $k=\pi/a$. In further experiments we will study the detailed dispersion of the dynamical response.

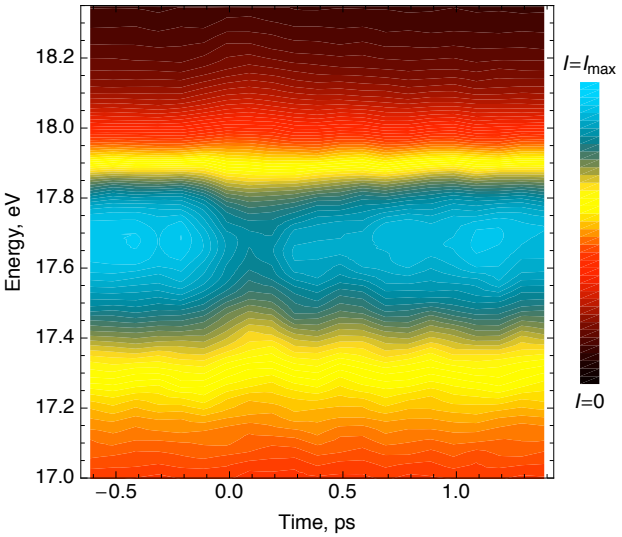

Fig. 1: Photoelectron intensity map of response to photoexcitation.

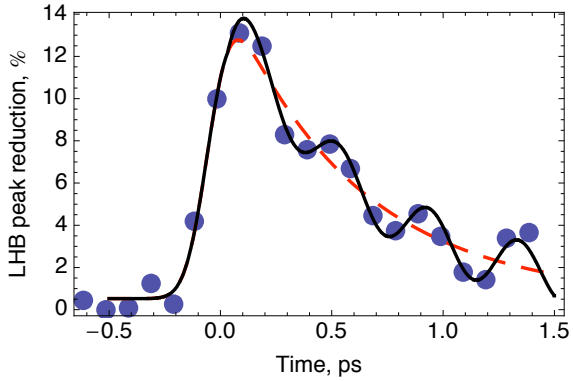

Fig. 2: Reduction in LHB intensity. Solid line: Full fit. Dashed line: Exponential component only.

Final Remarks

Artemis is uniquely suited to the task of understanding the relationship between CDW and Mott order in this material, and this will serve as an ideal first demonstration of the exciting possibilities offered by this new beam line.

References
1 E Dagotto, Science **309** 257 (2005)
2 Z Shen and D Dessau, Physics Reports **253** 1 (1995)
3 R Averitt and A Taylor, J. Phys.: Cond.Mat. **14** R1357 (2002)
4 L Perfetti *et al.*, Phys. Rev. Lett. **97** 067402 (2006)
5 K Rossnagel and N Smith, Phys. Rev. B **73** 073106 (2006)
6 J Demsar *et al.*, Phys. Rev. B **66** 041101R (2002).

Ultrafast time-resolved photoelectron imaging of excited state molecular dynamics: S_2-S_1 internal conversion in the DABCO molecule

Contact *j.underwood@ucl.ac.uk*

Roman Spesyvtsev and Russell S. Minns

Department of Chemistry, University College London, 20 Gordon St, London WC1H 0AJ

Marco Siano and Jon Marangos

The Blackett Laboratory, Imperial College London, Prince Consort Road, London SW7 2BW

Ruth Livingstone and David Townsend

School of EPS-Physics, Heriot-Watt University, Edinburgh EH14 4AS

Emma Springate and Edmond Turcu

Central Laser Facility, STFC Rutherford Appleton Laboratory, Didcot, Oxon OX11 0QX

David M. P. Holland

Photon Science Department ,STFC Daresbury Laboratory, Warrington WA4 4AD

Jonathan G. Underwood

Department of Physics and Astronomy, University College London, Gower Street, London WC1E 6BT

Introduction

The photodynamics of polyatomic molecules generally involves complex intramolecular processes which rapidly redistribute both charge and vibrational energy within the molecule. The coupling of vibrational and electronic degrees of freedom (resulting from the breakdown of the Born-Oppenheimer approximation) leads to radiationless processes such as internal conversion, isomerization, proton and electron transfer etc. These non-adiabatic dynamics underpin the photochemistry of almost all polyatomic molecules and are important in photobiological processes such as vision and photosynthesis, and underlie many concepts in active molecular electronics. If progress is to be made toward understanding and controlling molecular functionality it is clearly of fundamental importance to develop techniques to study and control non-adiabatic processes in complex molecular systems.

By virtue of its sensitivity to both electronic and nuclear configurations, femtosecond pump-probe time-resolved photoelectron spectroscopy has been shown to be a powerful and versatile probe of excited state photophysics. This technique allows electronic and nuclear motions to be disentangled, and in principle leaves no configuration of the molecule unobserved since ionization may occur for all molecular configurations [1]. This is in contrast to other techniques, such as absorption or fluorescence spectroscopy, which sample only certain areas of the potential energy surfaces involved, as dictated by oscillator strengths, selection rules and Franck-Condon factors. While a substantial amount of information is available from the evolution of the photoelectron energy spectrum in such experiments, significantly more information regarding the evolution of the molecular electronic symmetry is available from the photoelectron angular distribution (PAD) [1, 2] as measured in time-resolved photoelectron imaging (TRPEI) experiments. Here we report TRPEI measurements of the S_2-S_1 internal conversion dynamics in the 1,4-diazabicyclo[2.2.2]octane (DABCO – see Figure 1) molecule following photoexcitation to the S_2 state. Studies at different excitation wavelengths have allowed us to examine the dependence of the electronic relaxation dynamics upon vibrational energy of the molecule.

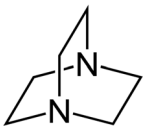

Figure 1: The DABCO molecule

Experimental setup

The experiments reported here were conducted at the Artemis facility at the Rutherford Appleton Laboratory. A schematic of the experiment is shown in Figure 2. TRPEI measurements were made using a velocity map imaging (VMI) photoelectron imaging spectrometer [3] equipped with a time and position sensitive delay line anode detector (Roentdek DLD40). An effusive inlet delivered DABCO vapour to the interaction region. During experiments the detector chamber pressure was maintained below 10^{-7} torr ensuring collisionless conditions.

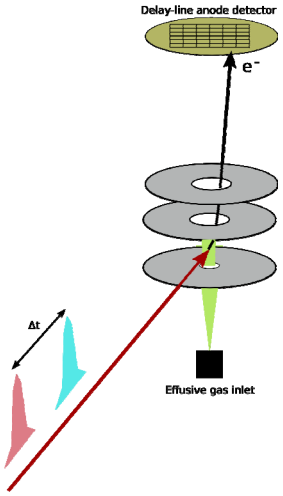

Figure 2: Schematic drawing of experiment. Pump and probe laser pulses interact with gaseous DABCO in the interaction point of a velocity map imaging spectrometer. The resulting electrons are accelerated to a time and position sensitive detector.

The pump and probe laser pulses were derived from a 1 kHz Ti:Sapphire CPA system (KM Labs Red Dragon) operating at 780 nm and delivering 30 fs pulses with 13 mJ pulse energy. The output of this laser system was split to produce synchronized pump and probe pulses. Tunable pump pulses in the region 236-252 nm were generated using a commercial OPA (Lightwave HE-TOPAS) and subsequent frequency mixing (signal plus pump followed by second harmonic generation) producing pulses with a duration of 40-50 fs and pulse energies up to 35 μJ. Probe pulses at 390 nm were obtained from frequency doubling of the output of the CPA system. For experiments employing a two-photon probe process, the output of the CPA system was used directly. Pump

and probe pulse energies were reduced to < 100 nJ using polarizers and half-wave plates as needed. Pump and probe pulses were recombined using an uncoated fused-silica flat with the UV pump pulse derived from the front surface (4%) reflection, and the probe pulse transmitted through the optic. Under these conditions on average less than one electron was produced per laser shot. The pump-probe time delay was adjusted using a motorized delay stage under computer control. Photoelectron images were obtained by collecting data for 0.25-2×10^6 laser shots.

Results

Figure 3 shows a representative photoelectron image obtained with a pump wavelength of 236.1 nm and single-photon ionization probe at 390 nm. Two distinct photoelectron bands are seen corresponding to ionization from the S_2 and S_1 electronic states of the molecule. Images were recorded as a function of pump-probe time delay, allowing us to follow the evolution from the S_2 state to the S_1 state. Figure 4 shows representative data of the population evolution in the two states obtained from a series of images at different time delays. In addition, we have information on the temporal evolution of the photoelectron angular distributions (not shown). Data was recorded for different pump wavelengths in the region 236.1-251.1 nm allowing us to examine the influence on the electronic dynamics of vibrational excitation in the S_2 state. In addition data was taken employing a two-photon probe ionization scheme at 780 nm. Analysis and interpretation of this data is ongoing.

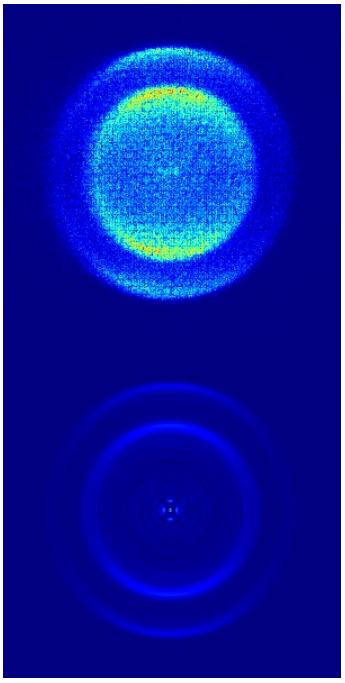

Figure 3: Photoelectron velocity map image recorded with a pump pulse at 236.1 nm and probe pulse at 390 nm. The raw experimental data is shown at the top, and the Abel inverted data is shown below. The outer ring corresponds to photoelectrons from ionization of the S_2 electronic state, and the inner ring corresponds to ionization of the S_1 electronic state.

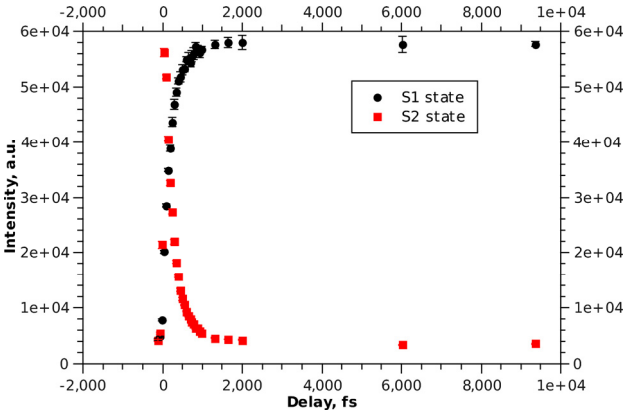

Figure 4: Populations of the S_2 and S_1 states as a function of pump-probe time delay following pump excitation at 236.1 nm.

Conclusions

Ultrafast time-resolved photoelectron imaging was applied to the study of internal conversion dynamics in the DABCO molecule as a function of internal energy. Analysis is ongoing.

Acknowledgements

We thank the CLF technical staff and particularly Steve Hook and Brian Landowski for technical support during this work.

References

1. A. Stolow and J. Underwood, Adv. Chem. Phys. **139**, 497 (2008).
2. J. G. Underwood and K. L. Reid, J. Chem. Phys. **113**, 1067 (2000).
3. A. T. J. B. Eppink and D. H. Parker, Rev. Sci. Instrumen. **68**, 3477 (1997).